RSC Advances

ROYAL SOCIETY
OF CHEMISTRY

www.rsc.org/advances

Understanding the local environment of Sm^{3+} in doped $SrZrO_3$ and energy transfer mechanism using time resolved luminescence: A combined theoretical and experimental approach

Santosh K. Gupta[a]*, P.S. Ghosh[b], Nimai Pathak[a], A. Arya[b], V, Natarajan[a]

a. Radiochemistry division, Bhabha atomic research centre, Mumbai-400085, India

b. Materials Science Division, Bhabha atomic research centre, Mumbai-400085, India

* Corresponding author. Tel.: +91-22-25590636; fax: +91-22-25505151.

E-mail address: santufrnd@gmail.com.

Abstract

A combined experimental and theoretical study on the photoluminescence (PL) properties of strontium zirconate (SZ) and Sm^{3+} doped SZ nanostructures is presented in this work. SZ and Sm^{3+} doped SZ is synthesized by Gel-combustion route and characterized systematically using X-ray diffraction (XRD), transmission electron microscopy (TEM) photoluminescence (PL) spectroscopy and electron paramagnetic resonance (EPR) experimental techniques. PL studies on nanocrystalline SZ shows strong violet blue and weak orange red emission under excitation wavelength at 243 nm. An EPR study shows the presence of oxygen vacancy in SZ nanocrystals. Combined emission, EPR studies and theoretical calculations brings out the possible reason for multicolor emission in SZ nanocrystals. The results of the PL spectroscopy measurement imply that the Sm^{3+} emissions, that originated from the $^4G_{5/2} \rightarrow$ ^6H_J (J = 5/2, 7/2, 9/2, and 11/2) intra-4f transitions of Sm^{3+} ions, are due to the indirect excitation of the Sm^{3+} ions through an energy transfer process from electron–hole pairs generated in the SZ hosts. Based on combined experimental and theoretical studies a possible mechanism of PL of undoped and Sm^{3+}-doped SZ is proposed.

Key words: $SrZrO_3$; Sm^{3+}; Defect; Luminescence; Energy transfer

1. Introduction

Amongst the plethora of inorganic structures, there is one that stands out through its versatility in derived structures and physical properties: the perovskite structure. Along with their related structures, perovskites have been widely studied for their interesting properties and have found many applications within an abundance of fields. As quoted by Stolen et al. [1] these structures have been termed an inorganic chameleon due to their large flexibility since the cubic mother structure easily distorts and adapts to the relative size of the ions forming the compound. The source of fascination is the diversity of the properties and their

high sensitivity to crystal chemical tuning; *i.e.*, a tiny change in chemical composition or/and crystal structure may induce huge changes in chemical and physical properties.

In particular, materials which represent the ABO_3 perovskite structure have constituted a central theme in the area of materials science and technology owing to their wide variety of potentially technological applications such as in solid oxide fuel-cells, as a proton conductor [2], magneto-resistors [3], in pigments industry [4], as a ferroelectric and dielectric materials [5-8], photocatalyst [9], luminescent materials [10, 11] and others. Recently, the $4d^0$ band insulator perovskite strontium zirconate (SZ) have attracted much attention as novel electronic materials. Because these materials have high melting points (over 2600^oC) [12], they can be used for high temperature devices, such as an electrochemical devices, due to their proton conductivity at fairly high temperatures [13].

Light emission from lanthanide ions plays an important role in solid state lighting (phosphor-converted light emitting diodes), display (plasma and field emission displays), and bioimaging (fluorescent markers) technologies. Owing to their high thermal and chemical stability and low environmental toxicity, lanthanide-doped alkaline-earth perovskite oxides of formula ABO_3 and their corresponding solid solutions $(A,A')(B,B')O_3$ (A, A′ = Ca, Sr, Ba; B, B′ = Ti, Zr, Hf) are attractive candidates for nanostructured phosphors for display and bioimaging technologies. Specifically, they have shown potential as phosphors for field emission [14] and electroluminescent [15] displays, and as fluorescent markers for bioimaging [16]. Recently lots of attention is given on the photoluminescent (PL) properties of titanates and zirconates with a disordered perovskite structure. The main reason is the distinct potential of these materials for electro-optic applications [17, 18]. The optical properties of disordered semiconductors are characterized by the presence of a broad PL band. This phenomenon is attributed to the electronic states inside the band gap, which are the main defects for an intense PL response. According to Longo et al., the displacement of Zr or Sr atoms in disordered perovskite $SrZrO_3$ may induce some vacancy defects at the axial and planar oxygen sites of the $[ZrO_6]$ octahedral [19]. It is well known that the vacancies defects may play important roles as luminescence centers and thus it is expected that the perovskite $SrZrO_3$ may show host emission. Defects induced violet blue emission from strontium zirconate host has been observed by many workers [10, 19, 20-22].

The ABO_3 type perovskite having various crystalline structures shows interesting physiochemical properties, which offer a potential host for the chemical substitution. Substitution at both A and B site can leads to change in symmetry and composition and thus create various defects viz. cation or oxygen vacancies which can drastically influence the

band structures and it's the main factor in determining the electronic structures. In particular, these materials can accommodate lanthanide ions on the A-site or B-site, and these doped oxides are not only used as a probe to investigate local centers and energy but also to provoke changes in their optical behavior. Moreover, doping foreign elements into a semiconductor with a wide band gap to create a new optical absorption edge is known to be one of the primary strategies for developing materials with optical-driven properties. However, the role of the rare earth (RE) in the perovskite structure is not really clear and is still being discussed.

Recently the lanthanide ion doped $SrZrO_3$ materials have been widely investigated due to their significance to fundamental research and their high potential for application in optical materials [23-30]. The luminescence efficiency of trivalent rare earth ions doped into inorganic matrices depends on the energy transfer from the host to the ion. It has been shown that the quantum efficiency from rare earth ions doped in nanocrystals increases as crystal size decreases [31]. The Sm^{3+} ion has a $4f^5$ configuration and therefore is labeled as a Kramer ion due to its electronic states that are at least doubly degenerate for any crystal field perturbation. Since samarium compounds have a narrow line emission profile and a long lifetime similar to europium compounds, they can be used as a probe in multianalytical assays.

$SrZrO_3$ has been prepared by several synthetic routes including solid-state reaction [32], sol-gel [33], co-precipitation [34] and hydrothermal methods [35]. The conventional solid state reaction route requiring temperatures in excess of 1400 K suffers from inhomogeneous and coarse sample formation with non uniform size distribution. Large and non-uniform phosphor particles are more likely to be prone to poor adhesion to the substrate and loss of coating. For good luminescence characteristics, phosphors should have small size, narrow size distribution, non-aggregation and spherical morphology. Similarly, several disadvantages have also been noted with the other synthetic techniques such as the evaporation of solvents resulting in phase segregation, alteration of the stoichiometry due to incomplete precipitation, expensive chemicals and time consuming processes. To overcome these limitations, a facile combustion synthesis route was suggested by Zhang et al., where the combustion reaction takes place at a lower temperature of 300^0C [27]. Through this method, a single phase compound could be synthesized without intermediate grinding or annealing steps.

Gel combustion is a novel method that uses a unique combination of the chemical Gel process and combustion. The Gel synthesis of ceramic oxides offers advantages such as high purity, good homogeneity, and low processing temperature. Combustion synthesis offers

advantages such as low energy requirements, simple equipment, and a short operation time because it uses a sustainable exothermic solid-solid reaction among the raw materials. The Gel combustion method is based on the gelling and subsequent combustion of an aqueous solution containing salts of the desired metals and an inorganic fuel such as acetylene black, and it yields a voluminous and fluffy product with a large surface area. This process has the advantages of inexpensive precursors, a simple preparation method, and the ability to yield nanosized powders. Most of the earlier luminescence reports on this ceramic host have been obtained with Eu, Ce or Dy as the activator ion.

However, when an active dopant is introduced into perovskite or structures with multiple sites (A and B), their optical and magnetic properties are dramatically changed depending on its distribution in the perovskite ceramic. Studies of dopant ion distribution in perovskite have attracted much attention because they may allow better understanding of the correlations between structure and properties such as color, magnetic behavior, catalytic activity, and optical properties, *etc.*, which are strongly dependent on the occupation of these two sites by metals **[36-39]**. None of the literature available explained the site symmetry of Ln^{3+} in $SrZrO_3$ nanocrystals. Considering the relatively wide band gaps, high refractive indices and lower phonon energy, SZ is a good candidate that can be used as host material for lanthanide ion luminescence in order to excite them efficiently and to yield intense luminescence. Metal ions could be conveniently substituted into the SZ lattice if their ionic radii are comparable to that of the Sr^{2+}/Zr^{4+} cations. Inserting dopants into SZ lattice should affect the photo-absorption behavior of SZ.

In this study, we have employed a combined experimental and first principle based theoretical approach to investigate in detail the local environment and energy transfer process in Sm^{3+} doped SZ. Time resolved emission spectroscopy (TRES), EPR and first principles based electronic density of state (DOS) calculations were used to explain defect induced emissions in nanocrystalline SZ. The luminescence efficiency of trivalent rare earth ions doped into inorganic matrices depends on the energy transfer from the host to the ion. So, time resolved fluorescence spectroscopy is used to identify the local environment around Sm^{3+} ion in SZ which is further validated by first principles based calculations. Finally, combining the experimental observation and theoretically calculated results, the energy transfer process of SZ host-to-Sm^{3+} is analyzed, and the corresponding mechanism is proposed.

2.0 Experimental

2.1. Sample preparation:

All the chemicals used in the sample preparation were of 'Analytical Reagent' grade and procured from Sigma Aldrich. Zirconyl oxychloride ($ZrOCl_2$), strontium nitrate $Sr(NO_3)_2$, ammonium nitrate (NH_4NO_3) and citric acid ($C_6H_8O_7 \cdot H_2O$) were used as starting materials for the synthesis in the molar ratio 1:1:10:1.25**.** First, $Sr(NO_3)_2$ and NH_4NO_3 were dissolved in quartz double distilled (QDD) water with stirring and then $ZrOCl_2$ solution was added to it. Under vigorous stirring, citric acid solution (2 M) prepared initially was poured into the mixed solution resulting an opal gel. This gel was dried at 100^oC for 10 h under IR lamp, and then transferred to a quartz beaker in a muffle furnace and kept at $300\ ^oC$ for 10 min. so as to form an ash-colored fluffy substance. In this step, the actual combustion reaction takes place using citric acid as the fuel. The ash-like product was then calcined at $600\ ^oC$ for 1 h. resulting in a white powder. The obtained white powders were ground and calcined at different temperatures.

For preparation of samarium doped sample (1.0 mol %), appropriate quantity of samarium nitrate were added at the initial stage prior to addition of $ZrOCl_2$ so that the final samarium concentration was 1.0 mol %.

2.2. Instrumentation:

The phase purity of the prepared phosphor was confirmed by X-ray diffraction (XRD). The measurements were carried out on a STOE X-ray diffractometer equipped with Ni filter, scintillation counter and graphite monochromator. The diffraction patterns were obtained using monochromatic Cu-K_α radiation (λ= 1.5406Å) keeping the scan rate at 1sec./step in the scattering angle range (2θ) of 10° to 60°. The $K_{\alpha2}$ reflections were removed by a stripping procedure to obtain accurate lattice constants. PL data were recorded on an Edinburgh CD-920 unit equipped with Xe flash lamp with 10-100 Hz frequency as the excitation source. The data acquisition and analysis were done by F-900 software provided by Edinburgh Analytical Instruments, UK. Time resolved emission studies (TRES) were carried out on an Edinburgh F-900 unit equipped with M 300 monochromator. The EPR spectra were recorded on a Bruker ESP-300 spectrometer operating at X-band frequency (9.5 GHz) equipped with 100 kHz field modulation and phase sensitive detection to obtain the first derivative signal. Diphenyl picrylhydrazyl (DPPH) was used for the calibration of g-values of paramagnetic species.

2.3. First-principles calculations:

Ab-initio calculations were performed using the plane wave based Vienna Ab-initio Simulation Package (VASP) [40-41]. VASP is based on the density functional theory (DFT) and we used generalized gradient approximation (GGA) for the exchange and correlation potentials as parameterized by Perdew, Burke and Ernzerhof (PBE) [42]. The projector augmented wave (PAW) potentials [43] were used for the ion-electron interactions including the valence states of Sr (4s, 4p, 5s - 10 valence electrons)), Zr (4s, 4p, 5s, 4d - 12 valence electrons), Sm^{3+} (5s, 5p, 4f, 6s - 11 valence electrons) and O (2s, 2p - 6 valence electrons). For orthorhombic $SrZrO_3$ (SZ) structure, optimization was carried out with respect to E_{cut} and k-point meshes to ensure convergence of total energy to within a precision of 0.1 meV/atom. The expansion of electronic wave functions in plane waves was set to optimized kinetic energy cut-off (E_{cut}) of 500 eV throughout this study. The Brillouin-zone (BZ) integrations were performed on an optimized Monkhorst-Pack [44] k-point grid of 12x12x8 for SZ and 4x4x4 for SZ supercells, respectively. The total energy of SZ was optimized with respect to volume (or lattice parameter), b/a, c/a ratio and atomic positions as permitted by the space group symmetry of the crystal structure. The structural relaxations (b/a, c/a ratio and atomic positions) were performed for each structure using the conjugate gradient algorithm until the residual forces and stress in the equilibrium geometry were of the order of 0.005 eV/Å and 0.01GPa, respectively. The final calculation of total electronic energy and density of states (DOS) were performed using the tetrahedron method with Blöchl corrections [45].

3. Results and discussion

3.1. Phase purity: PXRD

The XRD patterns of both $SrZrO_3$ and Sm doped $SrZrO_3$ samples annealed at 600^oC are shown in Figure 1. The patterns matched with orthorhombic phase of $SrZrO_3$ (ICDD file no 44-0161). Peaks due to impurities of $SrCO_3$ observed in the pattern (around $2\theta = 25^0$), are hardly avoided at such a low calcinations temperature and a short time. However, the existence of them seems to have little influence on the luminescence of $SrZrO_3$ [46]. The XRD data was indexed on an orthorhombic system with space group *Pnma* having cell parameters a = 5.817 Å, b=8.204 Å and c=5.797 Å. From the pattern of both undoped and doped sample, it can be inferred that incorporation of Sm in $SrZrO_3$ has not changed the crystal structure.

3.2. Morphological studies: HRTEM

Figure 2a shows high resolution transmission electron microscopy (HRTEM) micrographs of Sm^{3+} doped $SrZrO_3$ nanoparticles. HRTEM was utilized to examine the morphology of Sm^{3+} doped $SrZrO_3$ nanoparticles. Qualitatively, the material appears to be comprised of interconnected $SrZrO_3$: Sm particles that define cavities of mesoporous (20–50 nm) dimensions. The nanostructure is composed of spherical primary particles with features in the 2-5 nm range. These particles are connected to one another to form the larger clusters. The corresponding selected-area electron diffraction (SAED) pattern [Fig. 2(b)] confirmed the crystallinity of the sample, and indicated that nanocrystals are stabilized in a orthorhombic phase (Pnma) and are randomly oriented. Fig. 2(c) displays a high-resolution lattice image of Sm^{3+} doped $SrZrO_3$ nanoparticles, revealing the crystalline nature of the sample, further suggesting the absence of any parasite phase. Hence, the TEM studies confirmed the nanocrystalline nature of Sm^{3+} doped $SrZrO_3$ and ruled out the possibility of any samarium, strontium manganese or zirconium manganese precipitation.

The consecutive lattice fringes arranged in order even at the corner of a single particle without any crystalline border. The spacing of the observed lattice fringes was deduced to be 0.72 nm, which was associated with the (020) lattice plane of the orthorhombic phase of $SrZrO_3$.

3.3 Defect mediated emission in $SrZrO_3$

It is well-known that large number of defects exists in nanomaterials . Fig. 3 showed the room temperature photoluminescence spectra of $SrZrO_3$ nanoparticles. When exposed to 243 nm Xenon flash lamp, the sample exhibited visible light emission in a broad range of 400–635 nm. The most intensive photoluminescence peaks centered at 425 nm, implying violet-blue light emission. The PL profile is typical of a multiphonon process, i.e., emission that occurs by several paths and involves numerous states within the forbidden band gap. Considerable studies had verified that the photoluminescence properties of perovskite oxides of group IV elements stemmed from the oxygen vacancies and structural defects. Kan et al. reported that the photoluminescence intensity was directly related to the defects in the perovskite $SrTiO_3$ crystals and films [47]. Also, Longo et al. confirmed the defects related photoluminescence intensities through controlling the annealing temperature for perovskite $SrZrO_3$ and $BaZrO_3$ nanocrystals that were prepared by combustion method [19, 22, and 48]. The higher the calcining temperature, the more frequent the ZrO_6 conformation and the more ordered the structure. The yellow and red peaks decrease and the violet-blue peaks increase with heat treatment, since yellow-red emission is linked to the disordered structure and violet-blue to the ordered structure.

The visible spectrum wavelengths are usually between 400 nm and 700 nm. The energy carried by each visible photon is between 3.1 eV and 1.8 eV. Violet/blue color is more energetic than yellow/red/orange color. In our experiments, the intense violet and blue emission was therefore attributed to shallow defects in the band-gap and a more ordered structure, while the weak yellow and red emission was linked to defects deeply inserted in the band-gap and disorders in the lattice.

Therefore it can be concluded that in $SrZrO_3$, each colour has a different origin and are linked to a specific structural arrangement. When the sample was exposed to UV light, deep and shallow defects generated localized states in the band gap and non-homogeneous charge distribution formed traps for electrons. Due to the energy dependant localized levels, exciting the trapped electrons requires various energies. After excited, the blue luminescence originated from the recombination process in which an excited electron of the conductive band (CB) lost its energy and re-occupied the energy levels of an electron hole in the valence band (VB) through the localized defect levels.

3.3.2 Theoretical calculations

The calculated lattice parameters for SZ are a = 5.845 Å, b = 8.295 Å and c = 5.909 Å using GGA-PBE, which agree well with our XRD data of a = 5.797 Å, b = 8.204 Å and c = 5.817 Å and other experimentally determined values [49] within less than 1.5% deviations. Therefore, the GGA approximation is able to provide reliable results for the equilibrium lattice constants of the present system. The GGA-PBE calculated band gap for SZ is 3.7 eV which is not in agreement with the experimental value of 5.6 eV by optical conductivity analysis of the polycrystalline sample at room temperature [50]. But our calculated band-gap energy matches very well with previous GGA-PBE calculation of Z. Guo et al. [51]. The underestimation of band gap energy is a typical problem of DFT calculations in the GGA approximation. Nevertheless, the present calculations properly reproduce the good insulating character of ideal SZ.

Three structural models were built based on the ideal/ordered SZ structure (o-SZ) (Fig. 4) in order to simulate the disordered types and structural complex vacancies associated with them: (i) by displacement of the Zr (f-SZ); (ii) by displacement of Sr (m-SZ); and (iii) by simultaneous displacement Zr/Sr (fm-SZ) as described by V.M. Longo et al. [19]. The DOS were calculated with the total 0.5 Å vector displacement of the Zr and Sr network in all the dislocated models.

The calculated total and orbital angular momentum resolved DOS for o-SZ, f-SZ, m-SZ and fm-SZ are shown in Fig. 5, ranging from -4 eV below the top of the VB to 6 eV above and presenting the principles orbital states which influences the gap states. As seen in Fig. 5(a), the upper valence bands (VB) consist of O 2p states taking equivalent contributions from axial and planar oxygen atoms (shown in Fig. 4) with some additional contributions from Zr 4d states. The lower conduction bands (CB) are mainly Zr 4d states with some additional contributions from O 2p states. This clearly indicates covalent nature of Zr-O bonds and these DOS characters of SZ are consistent with the previous GGA results of Z. Guo et al. [51]. In the case of f-SZ (Fig. 5(b)), the VB is composed of O 2p states and the upper part of VB, i.e. the new states, is composed mainly of axial oxygen 2p states. In the m-SZ case (Fig. 5(c)), the upper part of VB is composed mainly of planner O 2p states. The fm-SZ structure shows a strong axial oxygen contribution in the new DOS present in the upper part of VB which is analogous to the f-SZ model. Moreover, the band gap energies of o-SZ, f-SZ, m-SZ and fm-SZ are 3.7, 2.96, 3.10 and 2.76 eV, respectively. The displacement in network former causes increased disorder in the lattice compared to the network modifier. The greater disorder occurs when both network modifier and former are displaced. This disorder is characterized by the reduction in band-gap energy in the disordered model [19]. Even though the numerical values of the GGA-PBE calculated band-gap energies of dislocation model structures are not correct but it follow the same sequence in which degree of disorder is present in these model structures. Therefore, the DOS features of o-SZ, f-SZ, m-SZ and fm-SZ are essentially similar to the DOS calculated by Longo et. al. [19] using DFT based calculations combined with the B3LYP hybrid functional. So the GGA-PBE methodology captures the essential features of structural defects and degree of disorder in SZ resulting from network former and modifier displacements.

The displacement in Zr (former) network promotes an increased disorder in the lattice when compared to the Sr (modifier) network. The greater disorder occurs when both the atoms are displaced. This disorder is characterized by the reduction in band-gap energy in the disordered model. The decrease in band gap in structurally disordered powder can be attributed to defects and/or local bond distortion, which yield local electronic levels in the band gap of this material. Increased disorder is linked to deep defects inserted in the band-gap and increased order is associated with shallow defects, which disappear when total order is reached. Increased disorder is due to presence of [ZrO_5. $V_O^{\cdot\cdot}$] and [ZrO_5. $V_O^{\cdot}$] complex clusters and are deeply inserted in the band-gap, leading to orange–red PL emission. [SrO_{11}.

$V_O^{\cdot\cdot}$**]** and [SrO$_{11}$. $V_O^{\cdot}$**]** complex clusters are linked to shallow defects in the band-gap and lead to a more energetic PL emission (violet–blue light) **[19]**. The deep defects linked to the Sr/Zr disorder are associated with the 2p states of axial oxygens and evidently shown in Figure 5(d). The shallow defects can be ascribed to the 2p states of planar oxygens in the VB as described in our DOS analysis. Increasing the lattice order causes these complex vacancies and the PL emission to disappear. The presence of oxygen vacancy is also confirmed by EPR studies as discussed in section 3.3.4

3.3.3. Excitation spectroscopy

To confirm that emission in SrZrO$_3$ is mediated by defect and is responsible for origin multicolor, we have recorded excitation spectra (Figure 6) corresponding to violet, blue, yellow and red emission. It was observed that excitation spectral feature remains same at entire wavelength range, dominated by a wide band center at about 246 nm (5.04eV), which indicates that the UV irradiation energy can be efficiently absorbed by SrZrO$_3$ host lattices and then is transferred to the emission centers. This band belongs to the host absorption band (HAB) and is generally ascribed to the charge transfer from the oxygen ligands to the central zirconium atom.

3.3.4. EPR spectroscopy

Electron paramagnetic resonance (EPR) shows a great potential for studying the local structure and properties of nanoparticles. It has to been noted that the influence of external factors on the radio-spectroscopic characteristics of nanosized and large (microns) particles is not identical since the charge state and other characteristics of intrinsic and impurity defects in nanoparticles depend on particle size and surface conditions.

The EPR spectrum of bare SrZrO$_3$ (Fig. 7), recorded after the final calcinations in air, is not a flat line (as one should expect in the case of the perfect stoichiometry) and shows an intense and asymmetric signal of the spin Hamiltonian at room temperature indicating the presence of some intrinsic defects in the as prepared material.

In the literature, this signal is related with singly ionized oxygen vacancies $V_O^{\cdot}$ and vacancy-related defects, **[52-54]** where the single asymmetrical peak *g* presents some variations of 1.9560–2.0030. We believe that the changes in *g* values are related to differences in the preparation method, chemical environment, and heat treatment conditions. The broad line width of signal indicates a certain degree of heterogeneity (several species differ slightly in spectral parameters) typical of disordered environments, such as those found

at the surface of nanostructured crystals. Even broader signals are found, for instance, for species formed at the surface of TiO_2 [55].

Matta *et al.* [56] used EPR measurements to verify the phase transformation from tetragonal to monoclinic zirconia and observed a signal $g = 2.0018$, which was attributed to trapped single electrons located in oxygen vacancies of ZrO_2. Lin *et al.* [57] reported that the EPR band at $g=1.9800$ is oxygen vacancy related. Thus, in the disordered structure, these $V_O^{\bullet}$ are linked to ZrO_5 clusters, called $[ZrO_5 \cdot V_O^{\bullet}]$ oxygen complex clusters [48].

3.3.5. Luminescence decay

Emission lifetimes were recorded using the time-correlated single-photon-counting (TCSPC) technique. Samples were excited with 243 nm laser pulses provided by the frequency-doubled output of Nd: YAG pumped OPO laser regenerative amplifier operating at a 10 Hz repetition rate.

The decay curves of $SrZrO_3$ annealed at $600^{\circ}C$ (as prepared sample) are shown in Figure 8 at excitation wavelengths of 243 nm monitoring emission at various wavelength on a 100 μs scale and fitted using the following exponential decay equation.

$$I(t) = A_o + A_1 \exp\left(\frac{-t}{\tau_1}\right) + A_2 \exp\left(\frac{-t}{\tau_2}\right) \qquad (1)$$

Here A_i are scalar quantities, t_i are the times of measurement and τ_i are the decay time values (i.e. the time taken for the excited state population to become 1/e of the original value. The decays measured here were all found to be multi-exponential in all the cases and could be adequately fit to a sum of two exponentials. The life-time values and % occupancy of each species obtained under different emission are given in Table 1. Broadly life time values obtained were ~2.00 and ~ 12.0 μs which are attributed to different types of defects present in bare $SrZrO_3$ nanocrystals. Slower decaying species was attributed to shallow defects in the band-gap and a more ordered structure whereas the faster decaying component is linked to defects deeply inserted in the band-gap and disorders in the lattice.

.

3.4. Excitation and Emission spectroscopy of Sm^{3+} doped $SrZrO_3$

Trivalent samarium ions emit a considerably bright luminescence in the visible and near infrared region in various kinds of host materials. The luminescence bands observed in

this ion emission are due to transitions between the energy levels in the $4f^5$ electron configuration. The excitation spectrum of the system at 597 nm emission is shown in figure 9. Broad band in the range of 200–275 nm and was assigned to the charge transfer band O^{2-} →Sm^{3+} (CTB) with λ_{max} at 243 nm. In the wavelength region 320–550 nm, several excitation peaks are observed and are located at 346 nm ($^6H_{5/2}$-$^6H_{13/2}$), 365 nm ($^6H_{5/2}$-$^4D_{3/2}$), 379 nm ($^6H_{5/2}$-$^6P_{7/2}$), 407 nm ($^6H_{5/2}$-$^4F_{7/2}$), 417 nm ($^6H_{5/2}$- $^6P_{5/2}$), 438 nm ($^6H_{5/2}$-$^4G_{9/2}$), 462 nm ($^6H_{5/2}$-$^4I_{9/2}$), 469 nm ($^6H_{5/2}$-$^4I_{11/2}$), 473 nm ($^6H_{5/2}$-$^4I_{13/2}$) and 485 nm ($^6H_{5/2}$-$^4I_{15/2}$) which are attributed to f–f transitions of Sm^{3+}. From the excitation spectrum, it was found that the intensity of f–f transition at 407 nm is high compared with the other transitions and has been chosen for the measurement of emission spectra of $SrZrO_3$: Sm^{3+} phosphors. The most intense peak at 407 nm clearly indicates that these phosphors are effectively excited by near ultraviolet light emitting diodes.

Emission spectra of Sm^{3+} ions doped $SrZrO_3$ with an excitation wavelength of 243 nm (CTB)/ 407 nm (f-f band) is shown in figure 10. Spectral features remain same on excitation with 250 nm (charge transfer) and 406 nm (f-f band). It is also noticed that, the intensities of emission bands are found to be low, when excited with the characteristic absorption band at 407 nm of Sm^{3+} ions, compared to that of emission intensities obtained with LMCT excitation band (250 nm). This may be due to the fact that the Sm^{3+} absorption bands corresponding to the f-f transitions are forbidden and exhibit poor absorptivities in UV region. The high intensities of emission bands when excited with LMCT are due to the intramolecular energy transfer (IMET) process, which occurs in the UV region.

The emission spectra consist of two parts: one is due to host in the region of 400-550 nm, another region comprising three sharp emission lines from 550 to 700 nm are the characteristic of the samarium ions. Three peaks are ascribed to the $^4G_{5/2}$-$^6H_{5/2}$, $^4G_{5/2}$-$^6H_{7/2}$ and $^4G_{5/2}$-$^6H_{9/2}$ transitions at 565, 597 and 643 nm of the Sm^{3+} ions, respectively. The peak at 703 nm is due to $^4G_{5/2}$-$^6H_{11/2}$ transition. Among these, the transition at 597 nm ($^4G_{5/2}$-$^6H_{7/2}$) is having the maximum intensity, which corresponds to the red emission of $SrZrO_3$:Sm^{3+} phosphors. It can be stated that the strong red emitting transition $^4G_{5/2}$-$^6H_{7/2}$ at 597 nm (ΔJ = ±1) is a partly magnetic dipole (MD) and partly electric dipole(ED) nature emission band. The other transition at 565nm ($^4G_{5/2}$-$^6H_{5/2}$) is purely MD natured and at 643 nm ($^4G_{5/2}$-$^6H_{9/2}$) is purely ED natured, which is sensitive to crystal field. Generally, the intensity ratio of ED and MD transition has been used to measure the symmetry of the local environment of the trivalent 4f ions. The greater the intensity of the ED transition, the more the asymmetry

nature. In our present study, the $^4G_{5/2}$-$^6H_{5/2}$ (MD) transition of Sm^{3+} ions is less intense than $^4G_{5/2}$-$^6H_{9/2}$ (ED) transition, indicating Sm^{3+} occupied asymmetric site in $SrZrO_3$.

We know that coordination number of Sr and Zr ions is 8 and 6 respectively. Since ionic size difference between 8-coordinated Sr^{2+} (126 pm) and 8-coordinated Sm^{3+} (108 pm) is less, Sm^{3+} ions occupying the Sr^{2+} sites will not lead to a large distortion in the lattice and if the associated defect due to charge difference is at a large distance, the local site symmetry will be having an inversion symmetry. On the other hand 6- coordinated Sm^{3+} with ionic size 96 pm while occupying 6-coordinated Zr^{4+} (ionic size 72 pm) has a larger size difference and can lead to distortion in the octahedra and the resulting in local site without inversion symmetry. On the other hand 6- coordinated Sm^{3+} with ionic size 96 pm while occupying 6-coordinated Zr^{4+} (ionic size 72 pm) has a larger size difference and can lead to distortion in the octahedra and the resulting in local site without inversion symmetry. Thus observed spectra where $^4G_{5/2}$-$^6H_{5/2}$ (MD) transition of Sm^{3+} ions is less intense than $^4G_{5/2}$-$^6H_{9/2}$ (ED) transition can be attributed to majority of Sm^{3+} ions occupying Zr^{4+} site without inversion symmetry though oxygen vacancies are introduced in vicinity to ensure local charge compensation. In $SrZrO_3$ the Zr^{4+} ion has the local symmetry D_{2h} within the ZrO_6 octahedron. However, the ionic radius of Sm^{3+} exceeds that of Zr^{4+} by about 24 pm (96 vs. 24 pm) and therefore induces a significant lattice distortion. From symmetry considerations it is known that in a noncubic environment a $^{2S+1}L_J$ manifold of RE^{3+} ion containing an odd number of electrons is split to J + 1/2 Stark levels with each level maintaining two-fold Kramers degeneracy [58]. Indeed, in the case of $^6H_{5/2}$ and $^6H_{7/2}$ the corresponding number of spectral lines can be counted. For $^6H_{9/2}$ and $^6H_{11/2}$ some of the transitions are probably too weak to be resolved. Splitting in the spectral line of Sm^{3+} further supports the fact that majority of samarium ion occupy low symmetric Zr^{4+} site.

3.5. Decay Time and TRES studies:

In $SrZrO_3$ perovskite structure the coordination numbers of Sr and Zr ions are 8 and 6 respectively as already discussed that can be occupied by the Sm^{3+} ions. To get an idea about the nature of the dopant ion occupancy in these lattice sites, PL decay time (life time) studies were conducted. The decay curves corresponding to the $^4G_{5/2}$ level of Sm^{3+} ions in the 1.0 mol % samarium doped $SrZrO_3$ shown in Figure 11 at excitation wavelength of 407 nm, monitoring emission at various wavelength viz. 565, 597 and 643 nm. For $SrZrO_3$:Sm^{3+}, a good fit was found to a biexponential decay using the similar equation as mentioned in equation (1).

The percentage occupancy of Eu^{3+} ions exhibiting a specific life-time is obtained in such case using the formula

$$\% \text{ of species (n)} = \left[\frac{(A_n \times \tau_n)}{\sum\limits_{n=1,2} A_n \times \tau_n} \right] \times 100 \ \% \tag{2}$$

Broadly, the analysis showed the presence of two components; one short lived and one long lived. In all the cases roughly the life time values were ~500 µs (short component, T_1, 75 %) and 1.6 ms (long component, T_2, 25 %) which can be indicative of the presence of two emitting species or states.

Makishima et al.[59] previously investigated the luminescence of Sm^{3+} in $BaTiO_3$ host lattice and found that the spectra consist of the two different series with various properties. They also found that some foreign ions can change the relative strength of the emissions of the two series owing to a charge compensation mechanism. On the basis of their results, they concluded that one series of the emissions is attributed to Sm^{3+} at the Ti^{4+} site, while the other series of emissions is related to the presence of Sm^{3+} in the Ba^{2+} site.

Assuming a given phonon energy (same host for the lanthanide ions), a relatively longer PL decay time should be attributed to a more symmetric site, as the f-f transition becomes more forbidden, whereas a shorter decay time is often associated with an asymmetric site due to relaxation in the selection rules. Species T_1 (500 µs) which is the major one arises because of Sm^{3+} ions occupying 6-coordinated Zr^{4+} site without inversion symmetry whereas minor species T_2 (1.6 ms) can be ascribed to Sm^{3+} ions occupying 6-coordinated Sr^{2+} with inversion symmetry. These results also corroborates our emission studies where we have observed that majority of Sm^{3+} ions occupying Zr^{4+} site without inversion symmetry. Such site selective spectroscopy of lanthanide in host like silicate, zirconate and pyrophosphate where multiple sites are available for occupancy has already been reported by our group [24, 25, 60-63].

In order to identify the environment associated with the species exhibiting different life-times, time resolved emission spectra (TRES) were recorded at different time-delays with constant integration time. Figure 12 shows the spectra recorded with time delays of 600 µs, and 3.0 ms respectively with integration time of 50 µs. As seen from the figure 10 after and giving a delay time of 600 µs; characteristic emission predominated by Sm^{3+} ions in asymmetric environment (Intensity $_{(643)}$ > Intensity $_{(597)}$) was observed. After delay time of 3.0

ms, the emission characteristics were overall similar to those observed after 600 µs delay with difference in intensity which is usually expected.

The spectra observed after 3.0 ms delay is expected from long-lived species (1.6 ms) as the other species would have reduced in intensity by a factor of e^{-6}. The spectra obtained after 600 µs delay time has contributions from both short-lived and long-lived species. The spectral characteristics of short lived species were obtained by subtracting the contribution of long-lived species (obtained mathematically using the spectra observed after 3.0 ms delay) from the observed spectra of 600 µs delay. Spectra for short lived and long lived species obtained after mathematical calculations are shown in the Figure 13. The $^4G_{5/2} \rightarrow {}^6H_{5/2}$ line is observed at 565, which originates from the magnetic dipole (MD) transition, and does not depend on chemical surroundings of the luminescent centre and its symmetry. However, the hypersensitive $^4G_{5/2} \rightarrow {}^6H_{9/2}$ transition at 643 nm is magnetic-dipole forbidden and electric-dipole allowed and its intensity increases as the environmental symmetry become lower. The asymmetry ratio was found to be 0.28 and 0.128 for short lived ($\mu = 500$ µs) and long lived ($\tau = 1.6$ ms) species respectively. This is in correspondence with phonon energy concept where short lived species will have more asymmetric component than long lived species.

3.6. Energy Transfer from Host to Rare-Earth Ions in SrZrO$_3$:Sm^{3+}

3.6.1. Luminescence Experiment

An obvious spectral overlap between the emission of host (oxygen-vacancy) and the excitation of Sm^{3+} can be observed, which is shown in Fig. 14. According to Dexter theory **[64]** an effective energy transfer (ET) requires a spectral overlap between the donor emission and the acceptor excitation. Consequently, the effective ET from the host to Sm^{3+} ions is expected. Therefore, the samples SrZrO$_3$ and SrZrO$_3$:Sm^{3+} were subjected into oxygen-deficient atmosphere (vacuum) to sinter with an attempt to observe the influence of the oxygen vacancies on the PL of the powders. We adopted vacuum atmosphere rather than reduction atmosphere sintering for preventing the reduction of Zr^{4+} in SrZrO$_3$ and SrZrO$_3$:Sm^{3+}. The results presented in Fig. 15 indicate that the sintering in vacuum is quite effective to improve the violet-blue emission of SrZrO$_3$ compared to emission intensity of air sintered sample as mentioned in earlier figure 3. It is safe to say that the vacuum-sintering in this study can create oxygen vacancies effectively. Comparing with the air-sintered SrZrO$_3$:Sm^{3+} phosphor (figure 10), the red emission intensity increased about 150% when the sample is sintered in vacuum. Based on the above results, we can suggest that the PL intensity enhancement in the vacuum-sintered SrZrO$_3$:Sm^{3+} phosphor is related to the creation

of the oxygen vacancies. To clarify the relation between the red emission and oxygen vacancies in the vacuum-sintered $SrZrO_3:Sm^{3+}$, we examine the emission (435 nm) of $SrZrO_3$ and $SrZrO_3:Sm^{3+}$, respectively. The results are shown in Fig. 15; the ET process from host (oxygen-vacancy) to Sm^{3+} can be confirmed as the violet-blue emission is largely decreased after Sm^{3+} doping into $SrZrO_3$. Consequently, in vacuum, the ET between the host and luminescence center (Sm^{3+}) becomes more effective, which lead to higher red emission intensity.

3.6.2. Electronic structure

To obtain a clear picture of the effect of samarium doping in ideal/ordered SZ, a 2x2x1 supercell (with 80 atoms) of o-SZ was modelled and one Sm atom is placed in Sr position (Sr-SZ), which correspond to doping level of 6.25 atom%. Another 2x2x1 supercell with one Sm atom placed in place of Zr atom was also modelled (Zr-SZ). Then these two structures were optimized with respect to volume, b/a, c/a ratio and atomic positions. Our GGA-PBE optimized equilibrium volume shows a reduction of 0.827 $Å^3$ and increase of 3.0 $Å^3$ for the Sr-SZ and Zr-SZ compared to o-SZ unitcell, respectively. In which ever position Sm goes, parent host structure remains orthorhombic and our XRD data for Sm doped SZ signifies this theoretical prediction.

To identify the localization of Sm ion in the distorted SZ (fm-SZ), two 2x2x1 supercell (80 atoms) of fm-SZ was modelled. In one case one Sm atom was placed in position of a Sr atom (Sr-fm-SZ) and in another case one Sm atom was placed in position of a Zr atom (Zr-fm-SZ), which corresponds to 6.25 atom% doping. Total DOS calculated with these Sm doped supercells are shown in Figure 16 (a) and (b). In both the cases the calculated band gaps, 2.69 eV for Sr-fm-SZ and 2.77 eV for Zr-fm-SZ (Fig. 16(a) and (b)), are comparable to the 2.76 eV for fm-SZ. Small change in the calculated band gap usually signifies small change in degree of order/disorder prevails in fm-SZ.

PL spectra of vacuum sintered $SrZrO_3:Sm^{3+}$ sample (Fig. 15) shows an energy transfer from host to Sm^{3+} at a higher wavelength compared to undoped $SrZrO_3$. In other words, Sm doping increases the disordering prevails in the host $SrZrO_3$. Therefore, localization of Sm atoms solely in the Sr position or in the Zr position is not justifying the increase of disordering in the host $SrZrO_3$. In order to further reveal possible localization of Sm ions, a 2x2x2 supercell (160 atoms) of fm-SZ was modelled and two Sm atoms were placed each in the Sr position and Zr position. Total DOS calculated with this Sm doped supercell is shown in Figure 16 (c) and the band gap of 2.2 eV can be evaluated from the

same. The reduced band gap compared to fm-SZ is manifestation of increase in disorder and it is justifying energy transfer from undoped $SrZrO_3$ to vacuum sintered $SrZrO_3:Sm^{3+}$ sample at higher wavelength. Thus, localization of Sm ions is most probable in both Sr as well as Zr position. These theoretical results are in complete agreement with our luminescence lifetime measurements as described in section 3.5. Also, the lifetime studies has shown the presence of Sm^{3+} in SZ nanocrystal having life time value of 500 µs and 1.6 ms corresponding to Sm^{3+} at Zr and Sr sites respectively.

The information about bonding mechanism could be provided by the partial DOS and Fig. 16 (c) shows partial DOS of Sm^{3+} doped both in Sr and Zr position of fm-SZ. Overall DOS for CB and VB of Sm^{3+} doped fm-SZ is similar to that of fm-SZ (as we described in Fig. 5 (d)). But the presence of some additional states in the band gap of Sm doped fm-SZ makes it different in the band gap region. The additional states in the upper part of VB (in the energy range -0.3 to 0 eV, scaled by Fermi energy (E_F)) are mainly contributed by the 4f-nonbonding states of Sm^{3+} placed in the position of Zr atoms of fm-SZ. Moreover, the additional states in the lower part of CB (in the energy range 2 to 2.25 eV, scaled by E_F) arise mainly from 4f-nondonding states of Sm^{3+} localized in the Sr position of fm-SZ. So the reduction in band gap of Sm^{3+} doped fm-SZ can be manifested from the presence of 4f-impurity states of Sm^{3+} in the band gap. Apart from the impurity states, the 4f-states of Sm^{3+} (localized at Zr position) are hybridize with O 2p-states in the energy range -4.2 eV to -0.25 eV. Importantly, the 4f-states of Sm^{3+} are concentrated in the energy range of -4.2 to -0.25 eV and 2.5 to 5 eV (scaled by E_F) and these energy ranges are also the lower VB portion and upper CB portion of the fm-SZ, respectively. Therefore, distribution of 4f-states of dopant Sm^{3+} are matching well with the Zr(d)-O(p) bonding states, Zr non-bonding d-states as well as defect states of host fm-SZ. Thus, the overlap of electronic DOS between host fm-SZ and Sm^{3+} doped fm-SZ makes the energy transfer process from host fm-SZ to Sm^{3+} doped fm-SZ feasible.

3.6.3. Photoluminescence mechanism in Sm^{3+} doped SZ

A combined experimental study and theoretical calculations enable us to give a further insight into the energy transfer and transition mechanism (shown in Figure 17). In Sm^{3+} doped fm-SZ, the absorption band is associated with excitation of oxygen-vacancy-trapped electrons from shallow and/or deep defect states (present in the top of the VB) to defect states present in the lower part of the CB. Subsequently, the photo excited electrons in the defect states of CB may migrate to the Sm^{3+} related multiple excited states through the process of

energy transfer, due to the energy match between the electronic states of fm-SZ and the energy states of Sm^{3+} (as shown in Figure 16 (c)). Finally, the excited photo-electrons at the excited f-states of Sm^{3+} could transfer to the long lived $^4G_{5/2}$ of Sm^{3+} via non-radiative relaxation, and then produce strong orange-red emission (combined by the emission of 565, 579, 643 and 703 nm) via radiative relaxation.

3.7. Materials Performance: Color coordinates

To evaluate the material performance on color luminescent emission, CIE chromaticity coordinates were evaluated for undoped and 1.0 mol% doped sample adopting standard procedures. The values of x and y coordinates of the system were calculated to be 0.202 and 0.166 respectively. This is represented as the point '*' in the CIE diagram shown in figure 18 (a). It is clear from the values that, strontium zirconate, give a 'violet-blue' emission. The color can be tuned to orangish-red emission (x = 0.550 and y = 0.375) on doping 1.0 mol% Sm^{3+} as shown in Fig. 18(b).

3.8. Radiative and non-radiative transition in $SrZrO_3:Sm^{3+}$ compared to pure Sm_2O_3 powder- Photoacoustic spectroscopy

The principle of photoacoustic (PA) spectroscopy is explained in our earlier work [65, 66]. The PA spectra of pure Sm_2O_3 and Sm^{3+} doped $SrZrO_3$ are shown in Fig.19. As compared to pure powder the PA spectra of $SrZrO_3:Sm^3$ is very weak and broad and moreover most of the transitions are missing. Pure samarium oxide shows very sharp PA spectra with lots of features. The PA spectra of Sm_2O_3 samples can reveal the absorption and relaxation processes of Sm^{3+}. The PA intensity spectrum of Sm_2O_3 at room temperature is shown in figure 19. It is distinguished by sharply defined and almost line like absorption band. Compared with the absorption spectra in solution, the PA spectrum is more complex and more intense.

In Fig. 18, the strongest PA band appears in the region of 400 and 471 nm which is attributed to the transition from the ground state to excited state $^4P_{3/2}$ and $^4I_{3/2}$ [67, 68]. This indicates that the superior relaxation process of $^4P_{3/2}$ and $^4I_{3/2}$ is non-radiative relaxation. The weaker PA bands in the region of 556 and 525 nm are attributed to the transition from ground state to the excited state $^4G_{5/2}$ and $^4F_{3/2}$ respectively. The $^4G_{5/2}$ level is the first excited state of Sm^{3+}, which means the radiative relaxation of $^4G_{5/2}$ is its prominent process. Since the $^4F_{3/2}$ level have many similarities with the $^4G_{5/2}$ level, the energy transferred to this level is easy to

be transferred to the $^4G_{5/2}$ level. So $^4G_{5/2}$ and $^4F_{3/2}$ are two radiative levels of Sm^{3+}. As it indicates in Fig. 19 the PA intensity correspond to these two levels is fairly weak.

Among the energy levels of Sm^{3+}, the longest-lived energy level is $^4G_{5/2}$ (about 6.26 ms) and it is also a strong fluorescence energy level **[69]**. The electron in the excited level $^4G_{5/2}$ has a high probability to take a radiative relaxation process. When the electrons are excited to higher energy levels such as $^4G_{7/2}$, $^4F_{3/2}$, usually they will relax to $^4G_{5/2}$ by a non-radiative process, and then relax by radiative process (fluorescence), which can be interpreted according to the model discussed by Y. Yang et.al. **[70]**. In Fig. 19 PA signals of those energy levels $^4G_{7/2}$, $^4F_{3/2}$, $^4G_{5/2}$ are so weak that we could just detect them where as excitation spectra shows all such transitions.

In doped sample PA intensity is very weak compared to pure powder. This study confirms that non-radiative component is negligible small in $SrZrO_3:Sm^{3+}$ and this can be a good candidate for near ultraviolet (~ 400 nm) light emitting diodes.

4. Conclusions:

In summary, $SrZrO_3$ and Sm^{3+} doped (1 mol %) $SrZrO_3$ nanoparticles sintered at 600° C were synthesized by gel-combustion method as well as characterized systematically using XRD, TEM and TRFS experimental techniques. Nanocrystalline SZ sample is showing defect induced intense violet blue and weak orange red emissions. Based on EPR and theoretical studies these defects were attributed to presence of shallow and deep defects, respectively. Their corresponding lifetimes were also calculated using PL decay measurements. On doping Sm^{3+} in SZ an efficient energy transfer takes place and Sm^{3+} ions are localized both in Sr and Zr positions of SZ. Theoretical calculation has also shown that incorporating Sm at individual site does not change the band gap at all; but incorporating Sm simultaneously at Sr and Zr site decrease the band gap by 0.7 eV. PL decay time shows the presence of two life time values in case of nanocrystalline $SrZrO_3:Sm^{3+}$: (i) Sm^{3+} at Zr^{4+} site (τ=500 µs) and (ii) Sm^{3+} at Sr^{2+} site (τ=1.2 ms) in the ratio of 3:1. Asymmetry ratio was found to be 0.28 and 0.128 for short lived (τ= 500 µs) and long lived (τ= 1.6 ms) species which is in accordance with phonon energy concept. It was also observed that Sm^{3+}-doping exhibit strong orange-red emissions (combined by the emission of 565, 595, 643 and 703 nm). The energy match between the electronic structure of SZ and energy levels of Sm^{3+} ions makes energy transfer from host SZ to Sm^{3+} feasible. The present phosphor is considered to be a novel red light emitting luminescent material with very low non-radiative decay probability.

References:

1. S. Stolen, E. Bakken and C.E. Mohn, *Phys. Chem. Chem. Phys.,* 2006, **8**, 429.

2. H. Iwahara, T. Yajima, T. Hibino and H. Ushida, *J. Electrochem. Soc.,* 1993, **140**, 1687

3. A.P. Ramirez, *J. Phys. Condens. Matter,* 1997, **9**, 8171

4. M. Jansen and H.P. Letschert, *Nature*, 2000, **404**, 980

5. R. Ramesh and N.A. Spaldin, *Nat. Mater.,* 2007, **6**, 21

6. J.F. Scott and C.A.P. De Araujo, *Science,* 1989, **246**, 1400

7. S. Mathews, R. Ramesh, T. Venkatesan and J. Benedetto, *Science,* 1997, **276**, 238

8. C.C. Homes, T. Vogt, S.M. Shapiro, S. Wakimoto and A.P. Ramirez, *Science,* 2001, **293**, 673

9. H. Iwakura, H. Einaga and Y. Teraoka*, Inorg. Chem.,* 2010, **49**, 11362

10. E. Longo et al., *Phys. Rev. B*, 2004, **69**, 1251151

11. V.M. Longo, L.S. Cavalcante, M.G.S. Costa, M.L. Moreira, A.T. de Figueiredo, J. Andres, J.A. Varela and E. Longo, *Theor. Chem. Acc.,* 2009, **124**,385

12. E. A. Slonimskaya and A. V. Belyakov, *Glass Ceram.* 2000, **58**, 54

13. R. A. Davies, M. S. Islam and J. D. Gale, *Solid State Ionics*, 1999, **126**, 323

14. A. Vecht, D. Smith, S. S. Chadha, C. S. Gibbons, J. Koh and D. Morton, *J. Vac. Sci. Technol.,* 1994, **12**, 781

15. H. Takashima, K. Shimada, N. Miura, T. Katsumata, Y. Inaguma, K. Ueda and M. Itoh, *Adv. Mater.,* 2009, **21**, 3699

16. R. Pazik, R. Tekoriute, S. Hakansson, R. Wiglusz, W. Strek, G. Seisenbaeva, Y. K. Gun'ko and V. G. Kessler, *Chem. Eur. J.,* 2009, **15**, 6820

17. B. Bouma and G. Blasse, *J. Phys. Chem. Solids,* 1995, **56**, 261

18. P. S. Pizani, H. C. Basso, F. Lanciotti, T. M. Baschi, F. M. Pontes, E. Longo and E. R. Leite, *Appl. Phys. Lett.*, 2002, **81**, 253

19. V.M. Longo, L.S. Cavalcante, R. Erlo, V.R. Mastelaro, A.T. De Figueiredo, J. R. Sambrano, S. de Lazaro, A.Z. Freitas, L. Gomes, N.D. Vieira Jr., J.A. Varela and E. Longo, *Acta Mater.,* 2008, **56**, 2191

20. D. J. Lee, D. H. Kim, J. W. Park and Y.S. Lee, *J. Korean Phys. Soc.,* 2011,**59** ,2797

21. J. W. Park , D. J. Lee, D. H. Kim and Y.S. Lee, *J. Korean Phys. Soc.,* 2011, **58** ,316

22. V. M. Longo, L.S. Cavalcante, A.T. De Figueiredo, L. P. S. Santos, E. Longo, J.A. Varela, J.R. Sambrano, and A.C. Hernandes, *Appl. Phys. Lett.,* 2007, **90** , 091906.

23. H. Zhang, X. Fu, S. Niu and Q. Xin, *J. Alloy Comd.,* 2008, **459**, 103

24. S. K. Gupta, M. Mohapatra, V. Natarajan and S.V.Godbole, *Int. J. Appl. Ceram. Technol.,* 2013, **10**, 593

25. S. K. Gupta, M. Mohapatra, V. Natarajan and S.V.Godbole, *J. Mater. Sci.* 2012, **47**, 3504

26. J. Huang, L. Zhou, Z. Wang, Y. Lan, Z. Tong, F. Gong, J. Sun and L. Li, *J. Alloys Compd.,* 2009, **487**, L5

27. A. Zhang, M. Lü, G. Zhou, Y. Zhou, Z. Qiu and Q. Ma, *J. Alloys Compd.,* 2009, **468**, L17

28. B.-B. Wang and W.-D. Yang *Adv. Mater. Res.* 2013, **679**, 3-8.

29. Y. Jin, Y. Hu, L. Chen, X. Wang, G. Ju and Z. Mou, *J. Am. Ceram. Soc.,* 2013, **96**, 3821

30. D.H. Kim, J.H. Kim, J.S. Chung and Y. Lee, *J. Nanosci. Nanotech.* 2013, **13**, 7572

31. R. Bazzi, M. A. Flores-Gonzalez, C. Louis, K. Lebbou, C. Dujardin, A. Brenier, W. Zhang, O. Tillement, E. Bernstein and P. Perriat, *J. Lumin.,* 2003, **445**,102

32. B. Popescu, S. Enache, C. Ghica and M. Valeanu, *J. Alloys Compd.,* 2011,**509**, 6395

33. C.Y. Liu and T.Y. Tseng, *J. Phys. D: Appl. Phys.,* 2007, **40**, 2157

34. H.S. Potdar, S.B. Deshpande, A.J. Patil, A.S. Deshpande, Y.B. Khollam and S.K. Date, *Mater. Chem. Phys.* 2000, **65**,178

35. M.M. Lencka, E. Nielsen, A. Anderko and R.E. Riman, *Chem. Mater.,* 1997, **9**, 1116

36. N. Pellerin, C. Dodane-Thiriet, V. Montouillout, M. Beauvy and D. Massiot, *J. Phys. Chem. B .,* 2007,**111**,12707.

37. V. Sepelak, S. Indris, I. Bergmann, A. Feldhoff, K.D. Becker and P. Heitjans, *Solid State Ionics.,* 2006, **177**, 2487.

38. L. Zou, X. Xiang, M. Wei, F. Li and D. G. Evans, *Inorg. Chem.,* 2008,**47**,1361.

39. A. Le Nestour, M. Gaudon, G. Villeneuve, M. Daturi, R. Andriessen and A. Demourgues, *Inorg. Chem.,* 2007, **46**, 4067.

40. G. Kresse, J. Furthmueller, *Phys. Rev. B* 1996, **5**, 11169.

41. G. Kresse, J. Furthmueller, *Comput. Mater. Sci.* 1996, **6**, 15.

42. J. P. Perdew, K. Burke, M. Enzerhof, *Phys. Rev. Lett.* 1996, **77**, 3685.

43. P. E. Blöchl, *Phys. Rev. B* 1994, **50**, 17953.

44. H. J. Monkhorst, J. D. Pack, *Phys. Rev. B* 1979, **13**, 5188.

45. P. E. Blöchel, O. Jepsen, O. K. Andesen, *Phys. Rev. B,* 1994, **4**, 16223.

46. A. Zhang, M. Lu, G. Zhou, Y. Zhou, Z. Qiu, Q. Ma, J. Alloy Compd., 2009, **468**, L17-L20

47. D. Kan, T. Terashima, R. Kanda, A. Masuno, K. Tanaka, S. Chu, H. Kan, A. Ishizumi, Y. Kanemitsu, Y. Shimakawa and M. Takano, Nat. Mater., 2005, 4, 816-829.

48. L. S. Cavalcante, V. M. Longo, M. Zampieri, J. W. M. Espinosa, P. S. Pizani, J. R. Sambrano, J. A. Varela, E. Longo, M. L. Simoes and C. A. Paskocimas, *J. Appl. Phys.,* 2008, **103**, 063527

49. B.J. Kennedy, C.J. Howard, B.C. Chakoumakos, *Phys Rev B*, 1999, **59**, 4023.

50. Y.S. Lee, J.S. Lee, T.W. Noh, D.Y. Byun, K.S. Yoo, K. Yamaura, *Phys Rev B* 2003, **67**, 113101

51. Z. Guo, B. Sa, J. Zhou, Z. Sun Z, *J. Alloys Compd*. 2013, 580, 148.

52. K. Vanheusden, W. L. Warren, C. H. Seager, D. R. Tallant, J. A. Voigt, and B. E. Gnade, *J. Appl. Phys*. 1996, **79**, 7983.

53. P. H. Kasai, *Phys. Rev.* 1963, **130**, 989.

54. M. Z. Z. Jin, J. Zhang, X. Guo, J. Yang, W. Li, X. Wang, and Z. Zhang, J.Mol. Catal. A: Chem. 2004, **217**, 203

55. S. Livraghi, M. Chiesa, M. C. Paganini, E. Giamello, *J. Phys. Chem. C,* 2011, **115**, 25413

56. J. Matta, J.-F. Lamonier, E. Abi-Aad, E. A. Zhilinskaya, and A. Aboukaïs, Phys. Chem. Chem. Phys. 1999,**1**, 4975.

57. C. Lin, C. Zhang, and J. Lin, J. Phys. Chem. C, 2007, **111**, 3300.

58. G.H. Dieke, Spectra and Energy Levels of Rare Earth Ions in Crystals, Interscience, New York, 1968.

59. S. Makishim, H. Yamamoto, T. Tomotsu, S. Shionoya, J. Phys. Soc. Jpn.1965, **20**, 2147

60. S. K. Gupta, M. Mohapatra, S. Kaity, V. Natarajan and S.V. Godbole, *J .Lumin.* 2012 **132**, 1329.

61. S. K. Gupta, M. Kumar, V. Natarajan and S.V. Godbole, *Opt. Mater.,* 2013, **35**, 2320

62. S. K. Gupta, M. Sahu, K. Krishnan, M. Saxena, V. Natarajan and S.V. Godbole, *J. Mater. Chem. C*, 2013, **1***,* 7054

63. S. K. Gupta, M. Mohapatra, V. Natarajan and S.V. Godbole, *RSC Advances,* 2013, **3**, 20046

64. D. Dexter, *J. Chem. Phys.,* 1953, **21**, 836

65. D. Chandrasekhar, S. K. Gupta, S.V. Godbole, *J. Mol. Struct.* 2013, **1051**, 95

66. S. K. Gupta, A.R. Dhobale, V. Natarajan, S.V. Godbole, *Spectrochim. Acta A*, 2014 **117**, 204

67. Y. Yuetao, Z. Shuyi, *J. Mol. Struct.* 2003, **646**, 103

68. S. Qingade, W. Qin, L. Jingci, N. Qida, *Spectrosc. Lett.* 1996, **29**, 1285

69. Yuetao Yang and Shuyi Zhang, *Spectrochim. Acta, Part A,* 2003, **59**, 1205

70. Y. Yang, Q. Su, G. Zhao, *Spectrochim. Acta, Part A,* 1998, **54**, 645

Table 1: Life time and % occupancy for the life time of SrZrO₃ host with different emission wavelength

λ_{em} (nm)	τ_1 in µs and (% occupancy for short lived species)	τ_2 in µs and (% occupancy for short lived species)
425 (violet)	1.85 (50)	13.9 (50)
468 (blue)	1.99 (49)	12.2 (51)
593(yellow)	2.00 (48)	11.7 (52)
615 (red)	2.14 (44)	10.4 (50)
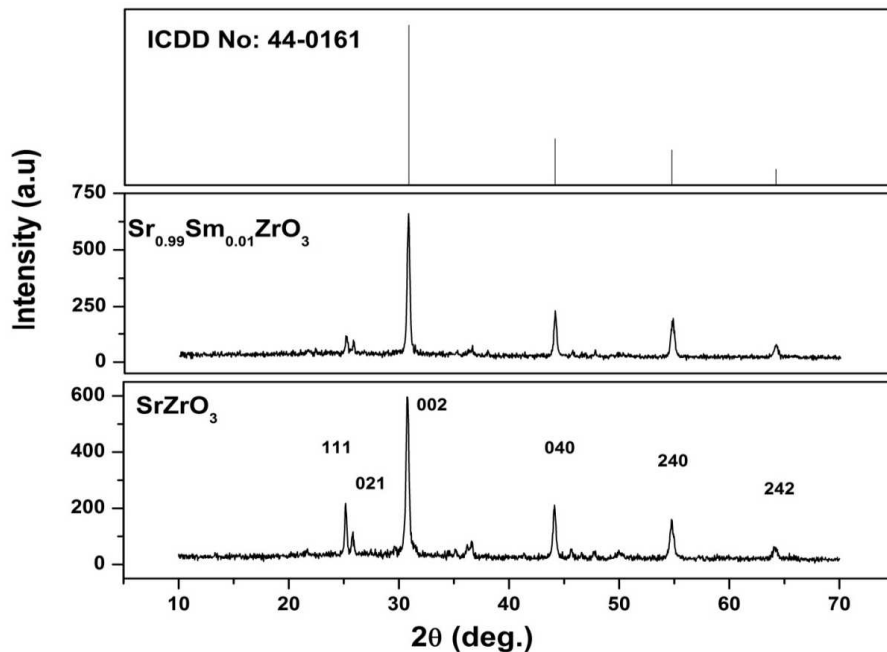
Figure 1: XRD patterns of the SrZrO$_3$ and Sm^{3+} doped SrZrO$_3$
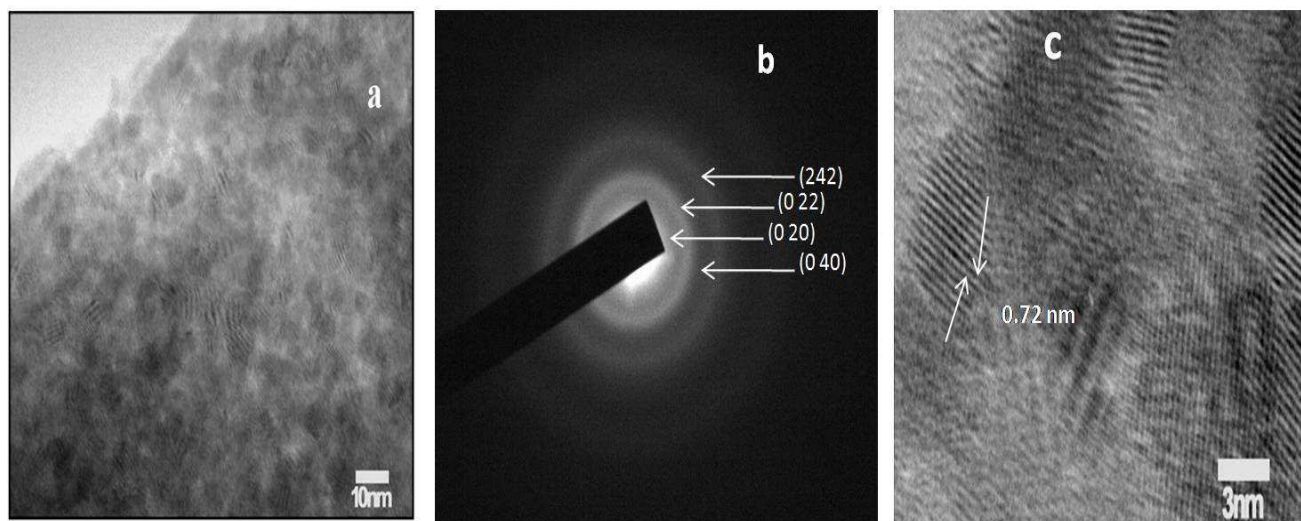
Figure 2: HRTEM micrographs of SrZrO$_3$:Sm^{3+} annealed at 600°C (as prepared samples) (a) Bright field image (b) Selected area electron diffraction and (c) High resolution image
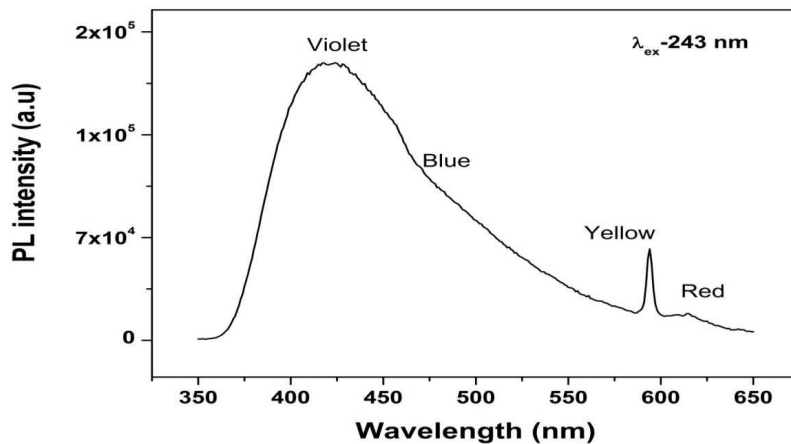
Figure 3: Emission spectra of air sintered $SrZrO_3$
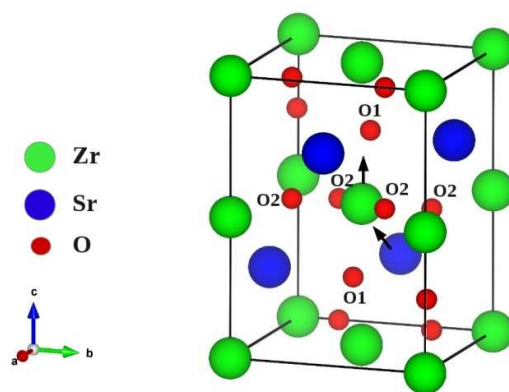
Figure 4: Schematic of $SrZrO_3$ unitcell. Arrows indicate direction of atomic displacement for the Zr and Sr network. O_1 and O_2 are the axial and planar oxygen atoms, respectively.
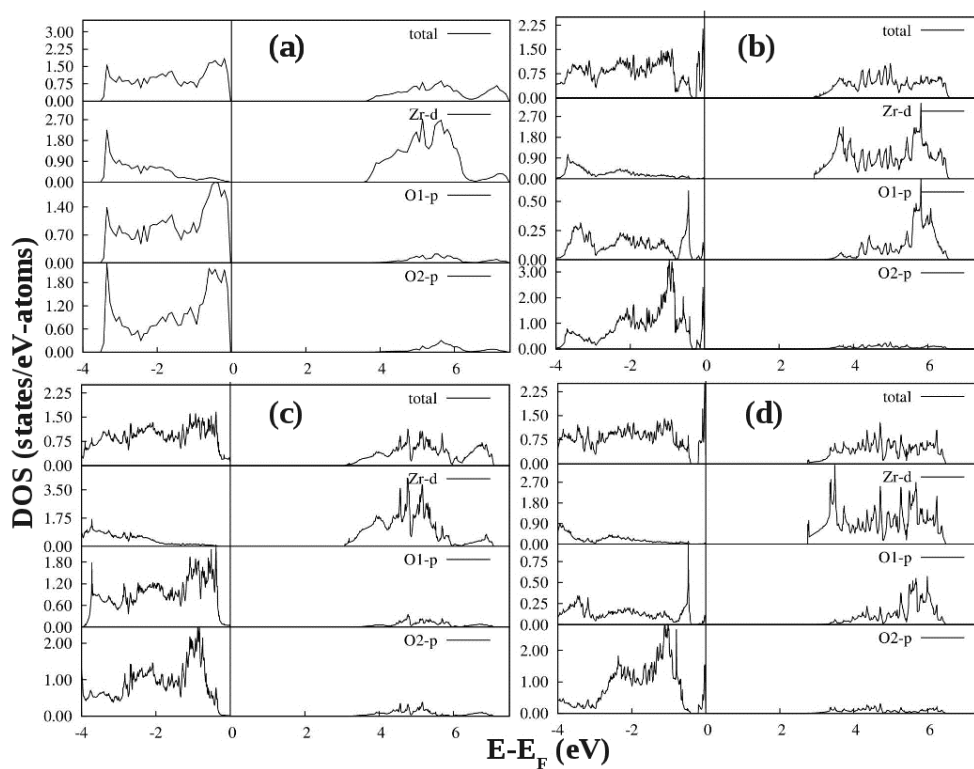
Figure 5: Total and orbital angular momentum projected DOS for: (a) o-SZ, (b) f-SZ, (c) m-SZ and fm-SZ models. The vertical lines represent Fermi level.
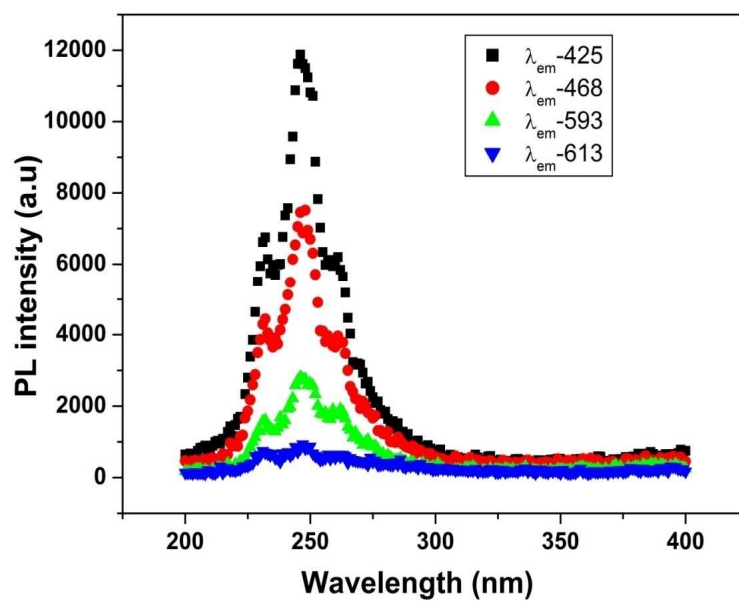
Figure 6: Excitation spectra of air sintered $SrZrO_3$ under different excitation wavelength
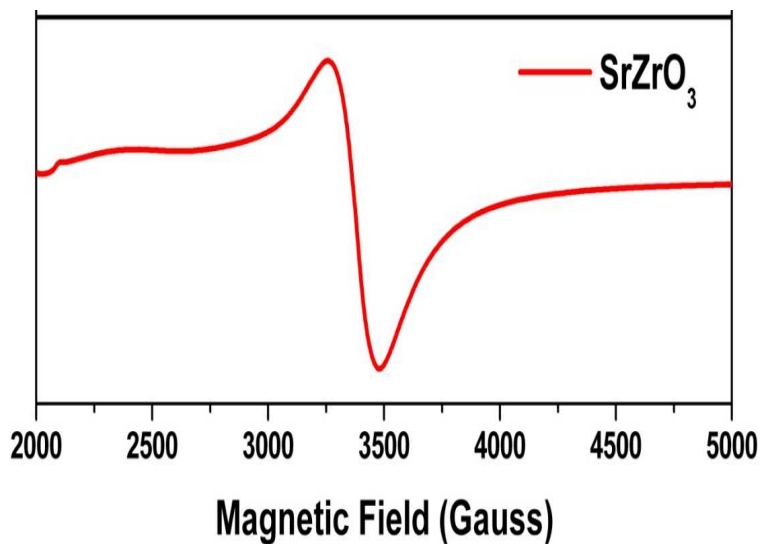
Figure 7: X-band EPR spectra of $SrZrO_3$ sample recorded at RT
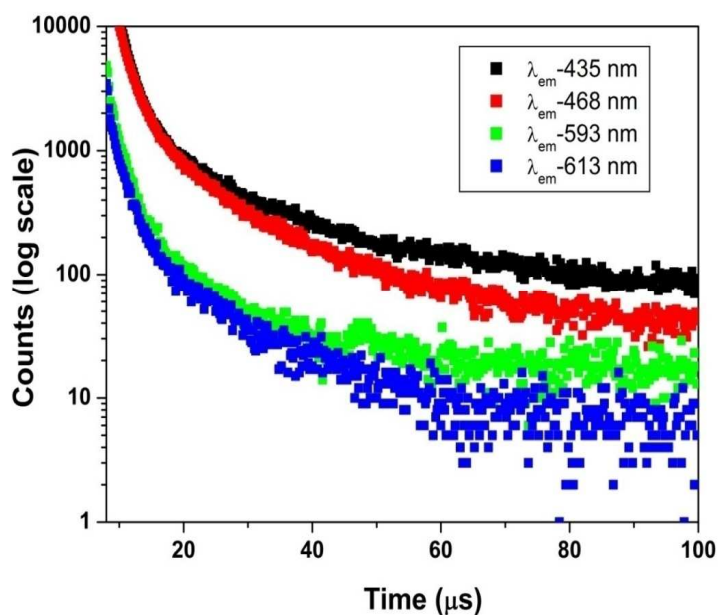
Figure 8: Decay curves of $SrZrO_3$ sample. Samples were excited at 243 nm and the emission was monitored at different wavelength.
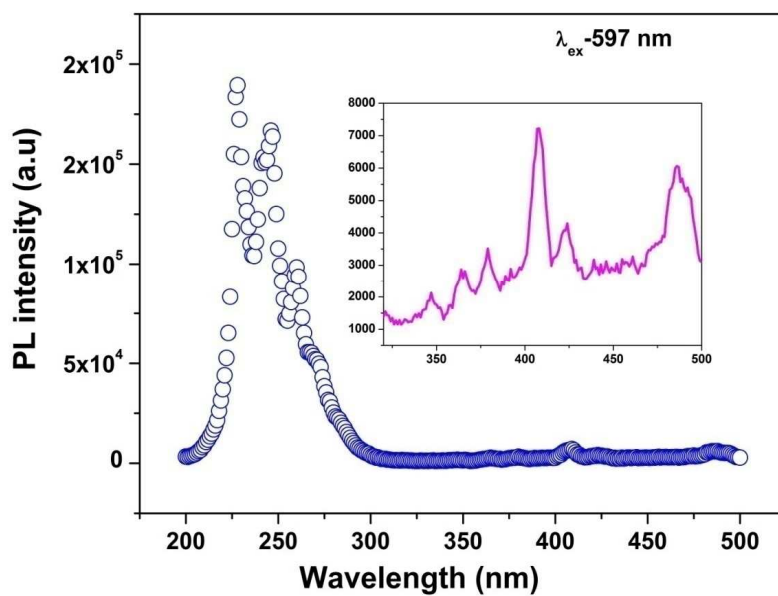
Figure 9: Excitation spectra $SrZrO_3:Sm^{3+}$. Inset shows the f-f lines of Sm^{3+}
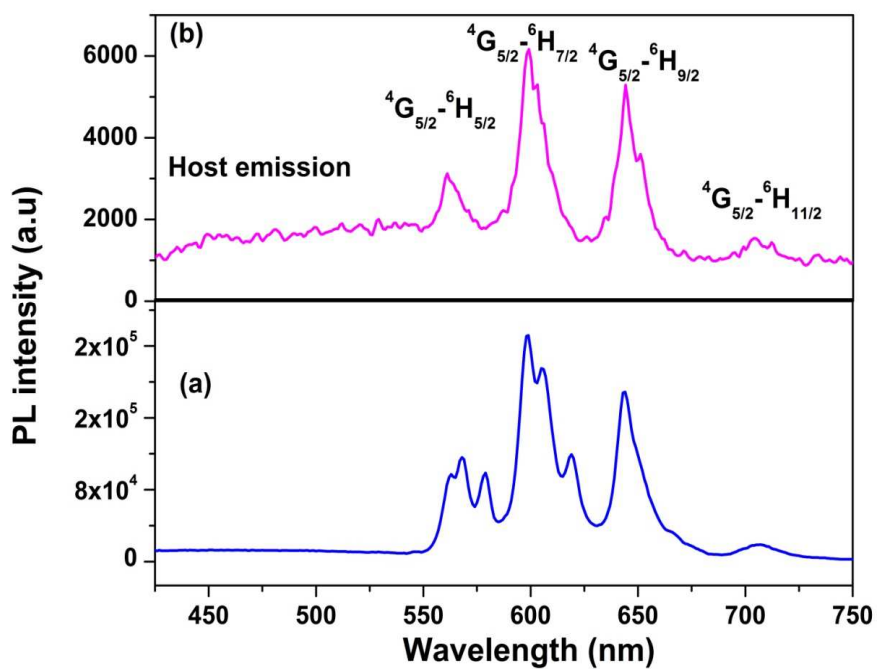
Figure 10: Emission spectra of air sintered $SrZrO_3$:Sm^{3+} at excitation wavelength (a) 243 nm (CTB) (b) 407 nm (f-f band)

.
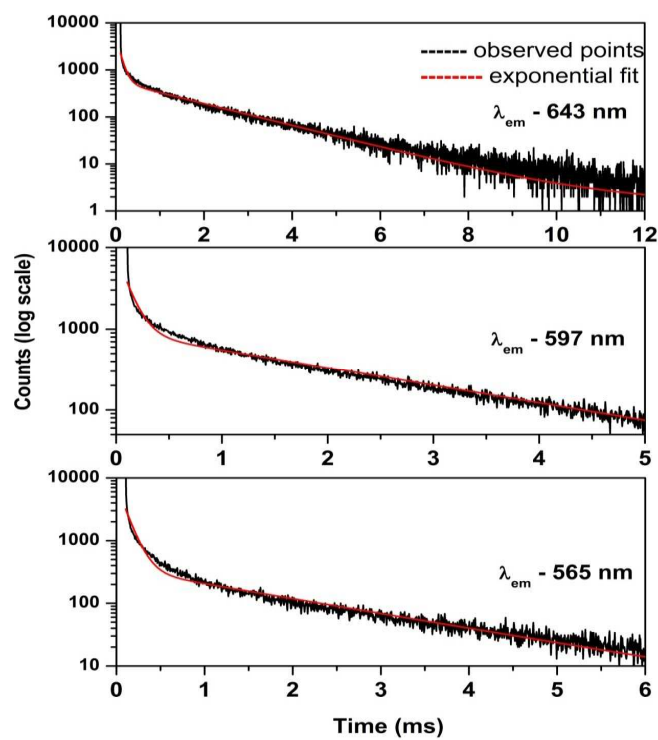
Figure 11: Luminescence decay time profile of $SrZrO_3$:Sm^{3+} at λ_{ex}-407 nm under λ_{em}-565, 597 and 643.
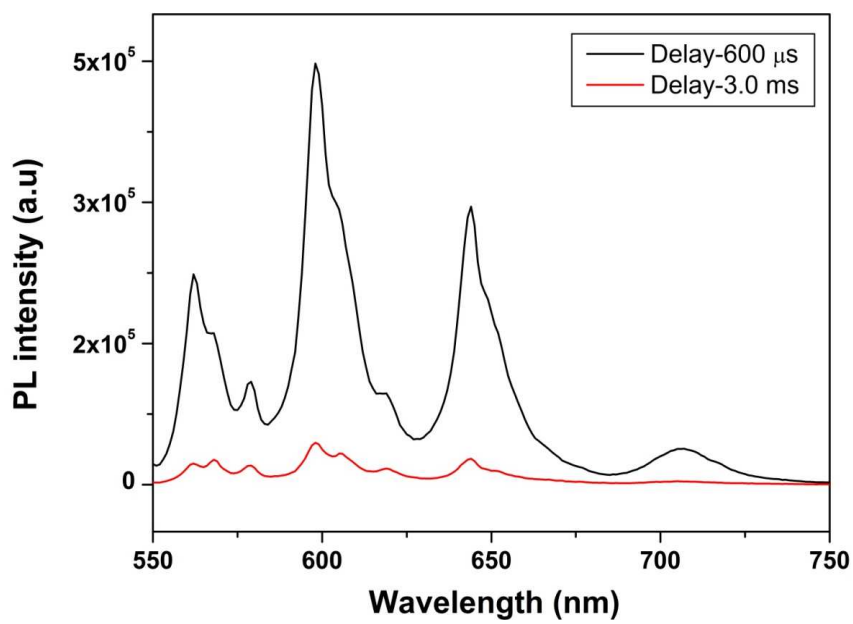
Figure 12: Time-resolved emission spectra of $SrZrO_3$:Sm^{3+} nanophosphor under the excitation at 243 nm (a) after giving suitable delay time
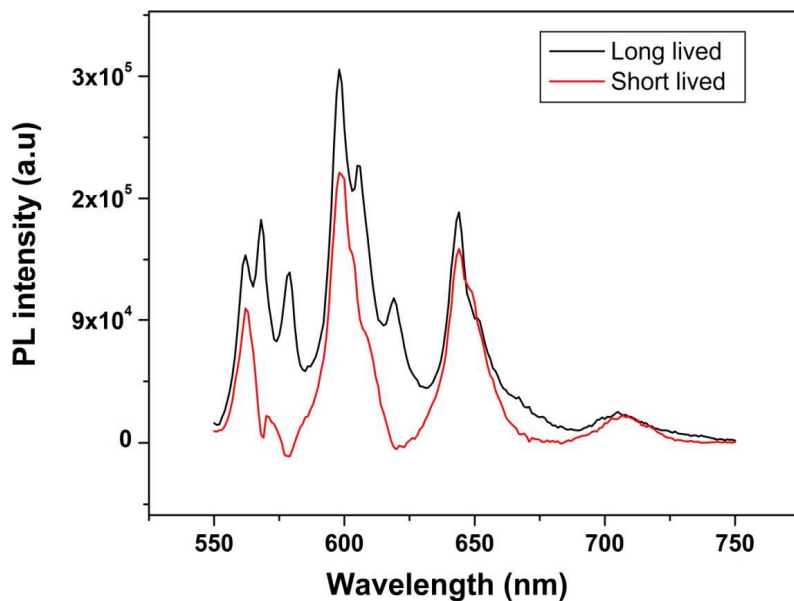
Figure 13: Time-resolved emission spectra of for short and long lived Sm^{3+} ion in $SrZrO_3$
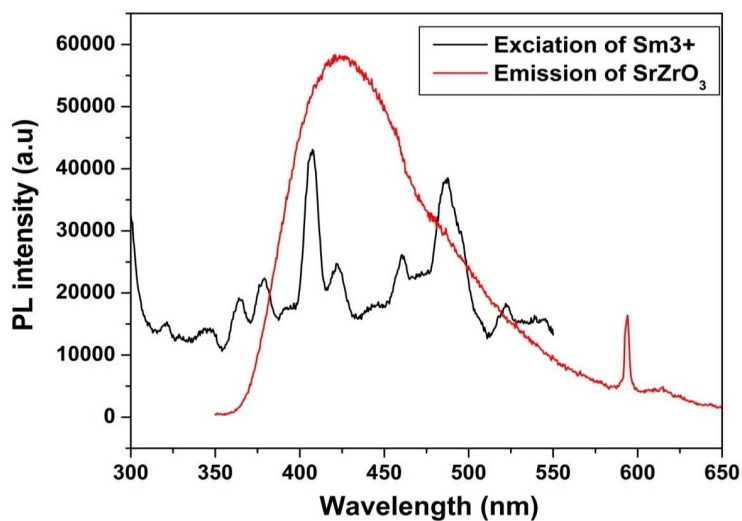
Figure 14: Emission spectra $SrZrO_3$ (λ_{ex}-243 nm) and excitation spectra of SrZrO3:Sm^{3+} (λ_{em}-597 nm)
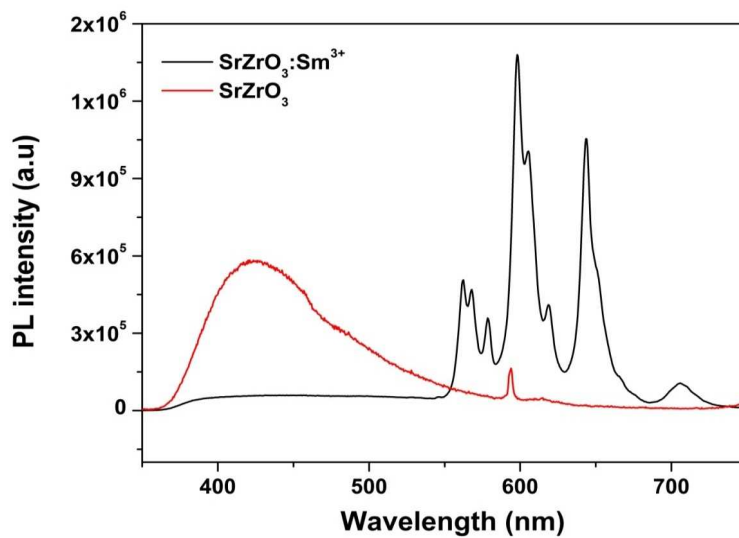
Figure 15: Energy transfer from host to Sm^{3+} ion (Vacuum sintered sample).
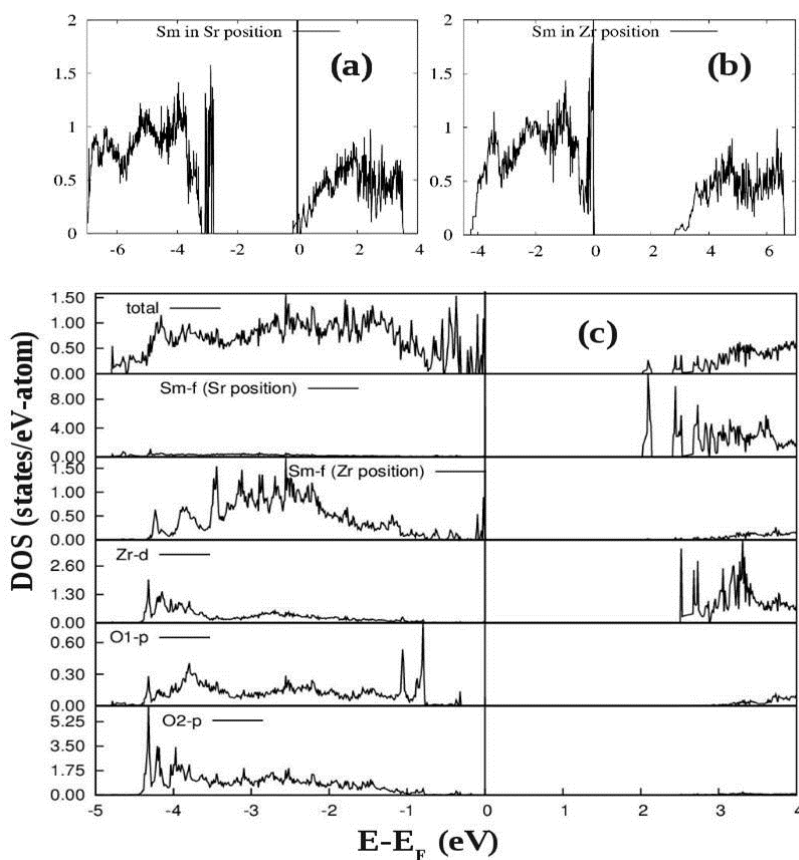
Figure 16: Total DOS for Sm doped fm-SZ in (a) Sr position and (b) Zr position. Total and partial DOS of Sm doped fm-SZ in both Sr and Zr position (c). The vertical lines represent Fermi level (E_F).
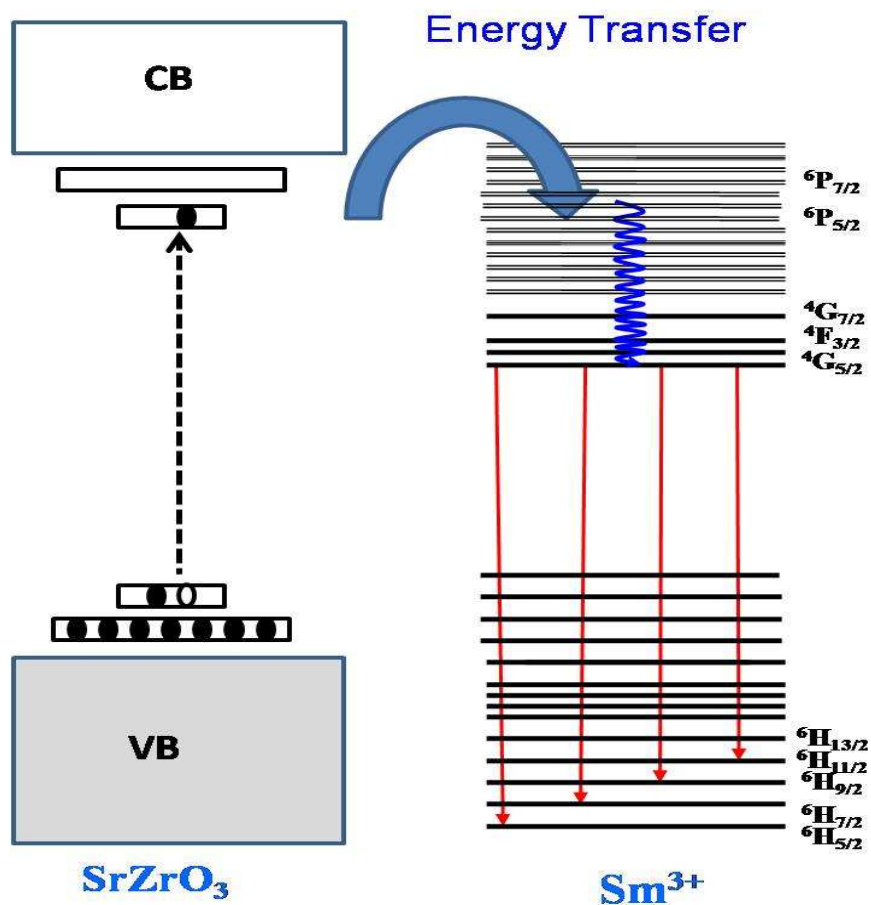
Figure 17: Schematic of energy transfer mechanism from $SrZrO_3$ host to Sm^{3+} ions.
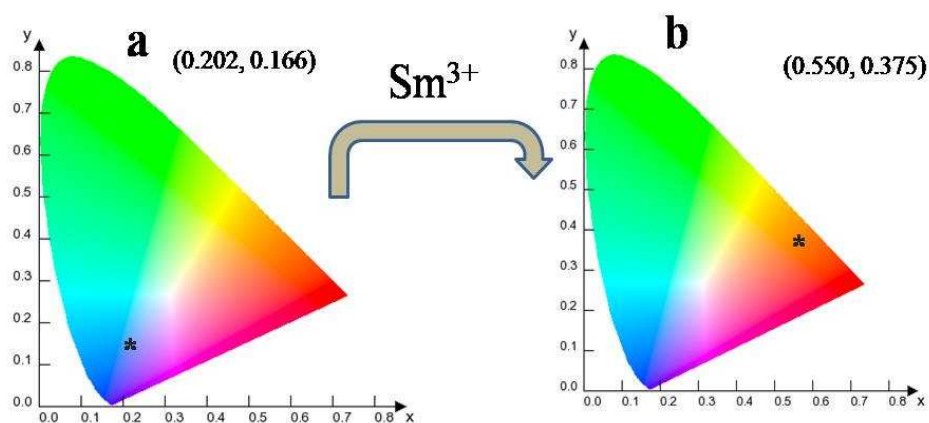
Figure 18: (a) CIE index diagram of (a) $SrZrO_3$ and (b) $SrZrO_3:Sm^{3+}$ system showing violet blue white and red emission (point *) respectively.

Fig.19. PA spectra of $SrZrO_3:Sm^{3+}$